



City Research Online

City, University of London Institutional Repository

Citation: Zhang, Z., Wu, Y., Jia, M., Song, H., Sun, Z. & Li, Y. (2017). MHD-RLC discharge model and the efficiency characteristics of plasma synthetic jet actuator. *Sensors and Actuators A: Physical*, 261, pp. 75-84. doi: 10.1016/j.sna.2017.03.039

This is the accepted version of the paper.

This version of the publication may differ from the final published version.

Permanent repository link: <https://openaccess.city.ac.uk/id/eprint/21648/>

Link to published version: <https://doi.org/10.1016/j.sna.2017.03.039>

Copyright: City Research Online aims to make research outputs of City, University of London available to a wider audience. Copyright and Moral Rights remain with the author(s) and/or copyright holders. URLs from City Research Online may be freely distributed and linked to.

Reuse: Copies of full items can be used for personal research or study, educational, or not-for-profit purposes without prior permission or charge. Provided that the authors, title and full bibliographic details are credited, a hyperlink and/or URL is given for the original metadata page and the content is not changed in any way.

City Research Online:

<http://openaccess.city.ac.uk/>

publications@city.ac.uk

MHD-RLC discharge model and the efficiency characteristics of plasma synthetic jet actuator

Zhibo ZHANG¹, Yun WU^{1,2*}, Min JIA¹, Huimin SONG¹, Zhengzhong SUN³, Yinghong LI¹

1 Science and Technology on Plasma Dynamics Laboratory, Air Force Engineering University, Xi'an, 710038, People's Republic of China

2 Science and Technology on Plasma Dynamics Laboratory, Xi'an Jiaotong University, Xi'an, 710049, People's Republic of China

3 Department of Mechanical Engineering and Aeronautics, City University London, London, United Kingdom

Abstract: Major factors affecting efficiency of plasma synthetic jet actuator (PSJA) are analysed based on a new discharge model in the present paper. The model couples the magnetohydrodynamics (MHD) equations with the resistor-inductor-capacitor (RLC) equations, and is able to resolve the time-dependent voltage fall on the sheath region and arc region, which is critical in analyzing energy loss in the heating process. This model is integrated into the commercial CFD software by a two-equation method. Results show that in a typical capacitive discharge at microsecond scale, the maximum energy loss is the sheath energy loss, which accounts for nearly half of the discharge energy, while the radiation loss is less than 5%. The discharge time is an important parameter for the PSJA efficiency. A short discharge time less than 1 microsecond will effectively reduce the sheath energy loss, while a longer discharge time will decrease the thermodynamic efficiency.

Keywords: plasma synthetic jet actuator; energy efficiency; MHD; gas discharge model

1 Introduction

The synthetic jet is a promising flow control method and a popular subject of many investigations. Based on a back-and-forth motion of a displacement object, the synthetic jet is easy to be generated. However, the moving component and its supporting components are relatively sensitive, and there is a general tendency to remove them and use a no-moving-parts instead. The first solution is to use the no-moving-part fluidic oscillator^[1-5]. However, for the oscillator actuator, the gas supply is necessary. Another actuator is the plasma actuators, which makes use of discharge to accelerate the gas. The dielectric barrier discharge (DBD) plasma actuator and plasma synthetic jet actuator (PSJA) are two representatives. The DBD features two flat electrodes flush mounted on either side of a dielectric^[6-8]. The PSJA consists of electrodes (anode and cathode) in a chamber with an orifice^{[9][10]}, as shown in Fig. 1. Different from DBD, the PSJA can generate high-speed jet, up to 100 m/s. In recent years, PSJA has shown promising capabilities in various applications such as control of shock wave/boundary layer interaction^{[11][12]}, shock wave manipulation^{[13][14]} and flight control^[15].

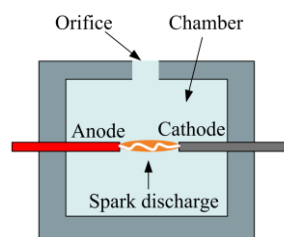


Fig. 1 The structure of the PSJA

However, PSJA has been suffering from the drawback of low efficiency. The efficiency of PSJA was estimated as 20-30%^[16] by Haack. An even lower efficiency of 4-10% was measured by a laser displacement sensor^[17]. Efficiency less than 5% was also reported in a few of numerical studies^{[18][19]}. The present work is thus to identify the reasons causing such low efficiency.

PSJA is an energy conversion device, which converts electric energy to jet mechanical energy. Following the energy flow of the PSJA operational cycle as shown in Fig. 2, the total efficiency consists of discharge efficiency, heating efficiency and thermodynamic cycle efficiency.

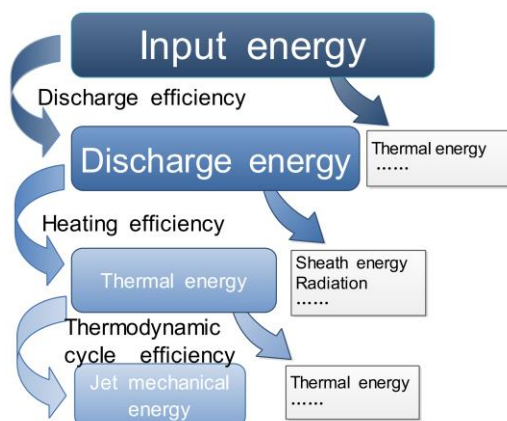


Fig. 2 Energy flow diagram of the PSJA

Substantial experimental and numerical works have been carried out to reveal the characteristics of the PSJA. In some early studies, the simplified model is widely used^{[20]-[24]}, where the heating process is ignored. The gas temperature in the PSJA cavity after discharge is calculated based on the constant volume heating theory. A model incorporating several heating power distribution laws by Taylor et al.^[25] was later proposed to investigate the temporal and spatial influences of heating power distribution. However, the distribution laws were given based on experience and they are hard to be validated experimentally. Hardy et al.^[26] included the resistor-inductor-capacitor (RLC) circuit model into the simulation by assuming the arc as a constant resistant. The ONERA group proposed a complete model of PSJA actuator, which contains more physical content, such as the real gas effect and discharge simulation. A more complex model coupled with RLC circuit was established by Dufour^[27]. In this model, the electric field is assumed to be homogeneous and oriented in the axial direction of the arc. A similar model was proposed by Laurendeau et al.^[28] recently, where the sheath resistance is assumed to be proportional to the arc resistance.

Reviewing on the existing models, the simulation of the heating process is critical to the accuracy, however, the majority of simulations focus on jet characteristics. In the present work, a discharge model coupling the MHD model with the typical RLC circuit is proposed to analyze the energy loss. In this model, the electric field is calculated by solving the potential conservation equation. The magnetic force induced by discharge current, the real gas effect, the sheath voltage fall, the radiation loss etc. are all taken into consideration. Based on this model, these energy loss factors are investigated in detail, including sheath energy loss, radiation loss, and energy loss in the heating process. At last, the influence of capacitance and inductance on the energy loss is discussed, and some suggestions for a higher efficiency PSJA are proposed.

2 Simulation model setup

This model includes two sub models, a MHD model^{[29]-[32]} and a RLC electrical model. The two sub models are connected with two variables, the voltage across the plasma region and the discharge current. The voltage across the plasma region consists of two main parts, the sheath voltage fall and the arc column voltage fall. In previous models, the arc column voltage fall is calculated based on the discharge current and the plasma resistance. In addition, the arc column resistance is obtained by integration method, which assumes that the electrical conductivity is independent on the axial direction,

and only changes along with the radial direction. Actually, in plasma region, the electrical conductivity distribution depends on the axial length. In this paper, the voltage across the plasma region is calculated by solving the potential conservation equation, which avoids the inaccuracy induced by calculating the plasma resistance. What's more, this model is easy to be applied to complex geometry structures.

2.1 Model establishment

2.1.1 Basic assumptions

To establish this simulation model, some assumptions must be made.

- A. The flow induced by arc discharge is axial symmetric. No sensible gains in model accuracy are reported when a more computational expensive three-dimensional approach is adopted^[33].
- B. The plasma meets local thermodynamic equilibrium (LTE) condition in the entire domain, so all the domain possesses the same temperature. Based on an energy balance equation, the evolution of the electron temperature and neutral particle's temperature with the pressure in arc discharge are plotted in Fig. 3. It is observed that plasma and air can be considered as fluid with same temperature, when the pressure is larger than 10 kPa. Therefore, the discharge in atmospheric pressure meets the LTE condition.

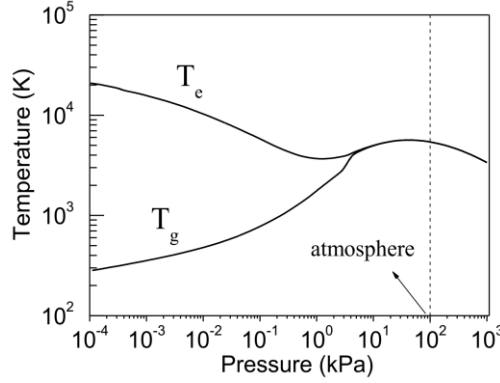


Fig. 3 Evolution of the electrons and heavy particles' temperature with the pressure

- C. The plasma is optically thin and radiation loss is modeled by a net emission coefficient. This is one of the simplest and most widely used methods for evaluating radiation loss in thermal plasma^{[34][36]}.
- D. Property parameters of the plasma are functions of the gas temperature and pressure, which is widely used in the arc simulation^{[18][28]}.
- E. The sheath voltage contains two parts, the anode fall and the cathode voltage fall. Based on the results of Zhou^[37], the cathode voltage fall is fitted as the function of the discharge current. The function is expressed as equation (1), and the fitting results are plotted in Fig. 4. The anode voltage fall is supposed to be proportional to the cathode voltage fall. The proportional coefficient is set as 0.3, based on the results of Hemmi^[38]. So the voltage across the plasma region u_p is indeed the sum of the calculated voltage difference $u_{a,c}$ between the cathode and the anode based on MHD model and the voltage fall on sheath, which is calculated by equation (2).

$$u_c = 22.64 \exp\left(-0.273 |I|^{0.5882}\right) + 11.62 \quad (1)$$

$$u_p = 1.3u_c + u_{a,c} \quad (2)$$

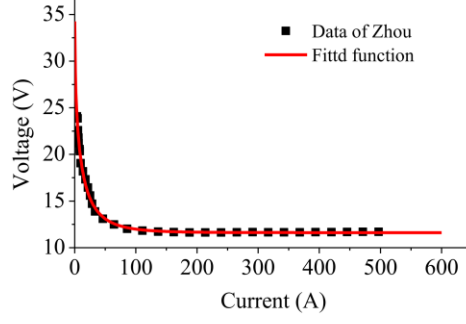


Fig. 4 Evolution of the voltage fall on sheath with the discharge current

2.1.2 MHD model

Based on the above assumptions, the transport equations in axisymmetric coordinate system can be written as follows.

Mass conservation equation:

$$\frac{\partial \rho}{\partial t} + \frac{\partial}{\partial x}(\rho v_x) + \frac{\partial}{\partial r}(\rho v_r) + \frac{\rho v_r}{r} = 0 \quad (3)$$

Axial and radial momentum conservation equations:

$$\begin{cases} \frac{\partial}{\partial t}(\rho v_x) + \frac{1}{r} \frac{\partial}{\partial x}(r \rho v_x v_x) + \frac{1}{r} \frac{\partial}{\partial r}(r \rho v_x v_r) = -\frac{\partial p}{\partial x} + \frac{1}{r} \frac{\partial}{\partial x} \left[r \mu \left(2 \frac{\partial v_x}{\partial x} - \frac{2}{3} (\nabla \cdot \mathbf{v}) \right) \right] + \frac{1}{r} \frac{\partial}{\partial r} \left[r \mu \left(2 \frac{\partial v_x}{\partial r} + \frac{\partial v_r}{\partial x} \right) \right] + j_x B_\theta \\ \frac{\partial}{\partial t}(\rho v_r) + \frac{1}{r} \frac{\partial}{\partial x}(r \rho v_x v_r) + \frac{1}{r} \frac{\partial}{\partial r}(r \rho v_r v_r) = -\frac{\partial p}{\partial r} + \frac{1}{r} \frac{\partial}{\partial x} \left[r \mu \left(\frac{\partial v_x}{\partial x} + \frac{\partial v_r}{\partial r} \right) \right] + \frac{1}{r} \frac{\partial}{\partial r} \left[r \mu \left(2 \frac{\partial v_r}{\partial x} - \frac{2}{3} (\nabla \cdot \mathbf{v}) \right) \right] - 2 \mu \frac{v_r}{r^2} + \frac{2}{3} \frac{\mu}{r} (\nabla \cdot \mathbf{v}) - j_r B_\theta \\ \nabla \cdot \mathbf{v} = \frac{\partial v_x}{\partial x} + \frac{\partial v_r}{\partial r} + \frac{v_r}{r} \end{cases} \quad (4)$$

Energy conservation equation:

$$\begin{aligned} \frac{\partial}{\partial t}(\rho E) + \frac{\partial}{\partial x}(u_x \rho h) + \frac{1}{r} \frac{\partial}{\partial r}(r u_r \rho h) &= \frac{\partial}{\partial x} \left(\frac{k_{eff}}{C_p} \frac{\partial h}{\partial x} \right) + \frac{1}{r} \frac{\partial}{\partial r} \left(r \frac{k_{eff}}{C_p} \frac{\partial h}{\partial r} \right) + v_x \frac{\partial p}{\partial x} + v_r \frac{\partial p}{\partial r} + \\ \mu \left\{ 2 \left[\left(\frac{\partial v_r}{\partial r} \right)^2 + \left(\frac{v_r}{r} \right)^2 + \left(\frac{\partial v_x}{\partial x} \right)^2 \right] + \left(\frac{\partial v_r}{\partial x} + \frac{\partial v_x}{\partial r} \right)^2 - \frac{2}{3} \left[\frac{1}{r} \frac{\partial}{\partial r}(r v_r) + \frac{\partial v_x}{\partial x} \right]^2 \right\} &+ \frac{j_x^2 + j_r^2}{\sigma} - 4 \pi \varepsilon_n + \frac{5}{2} \frac{k_b}{e} \left(\frac{j_x}{C_p} \frac{\partial h}{\partial x} + \frac{j_r}{C_p} \frac{\partial h}{\partial r} \right) \end{aligned} \quad (5)$$

Potential conservation equation:

$$\frac{\partial}{\partial x} \left(\sigma \frac{\partial V}{\partial x} \right) + \frac{1}{r} \frac{\partial}{\partial r} \left(r \sigma \frac{\partial V}{\partial r} \right) = 0 \quad (6)$$

Axial and radial vector potential conservation equations:

$$\begin{cases} \frac{\partial}{\partial x} \left(\frac{\partial A_x}{\partial x} \right) + \frac{1}{r} \frac{\partial}{\partial r} \left(r \frac{\partial A_x}{\partial r} \right) = -\mu_0 j_x \\ \frac{\partial}{\partial x} \left(\frac{\partial A_r}{\partial x} \right) + \frac{1}{r} \frac{\partial}{\partial r} \left(r \frac{\partial A_r}{\partial r} \right) = -\mu_0 j_r + \frac{A_r}{r^2} \end{cases} \quad (7)$$

In the above equations, ρ and p denotes density and pressure respectively; \mathbf{v} represents the velocity, v_x and v_r stands for the axial and radial velocity respectively; E is the internal energy; h stands for the enthalpy; κ_{eff} represents the thermal conductivity; ε_n denotes the net emission coefficient, which is obtained from [39] for one atmosphere, and values for other pressures are got by multiplying the ratio of local pressure to one atmosphere pressure^[40]; k_b stands for Boltzmann constant; e is the elementary charge, σ represents the electrical conductivity. B_θ is the magnetic field, which is calculated by equation (8); the current density components j_x and j_r can be deduced from the potential, as equation (9).

$$B_\theta = \frac{\partial A_r}{\partial x} - \frac{\partial A_x}{\partial r} \quad (8)$$

$$\begin{cases} j_x = -\sigma \frac{\partial V}{\partial x} \\ j_r = -\sigma \frac{\partial V}{\partial r} \end{cases} \quad (9)$$

To solve these conservation equations, the gas state equation must be added. The calculated results of Angola et al. are used^[41]. Based on these fitting equations, the thermodynamic and transport properties of high temperature equilibrium air plasma can be calculated in a wide range of pressures (0.01-100 atm) and temperatures (50-60000 K). Main results are plotted in Fig. 5.

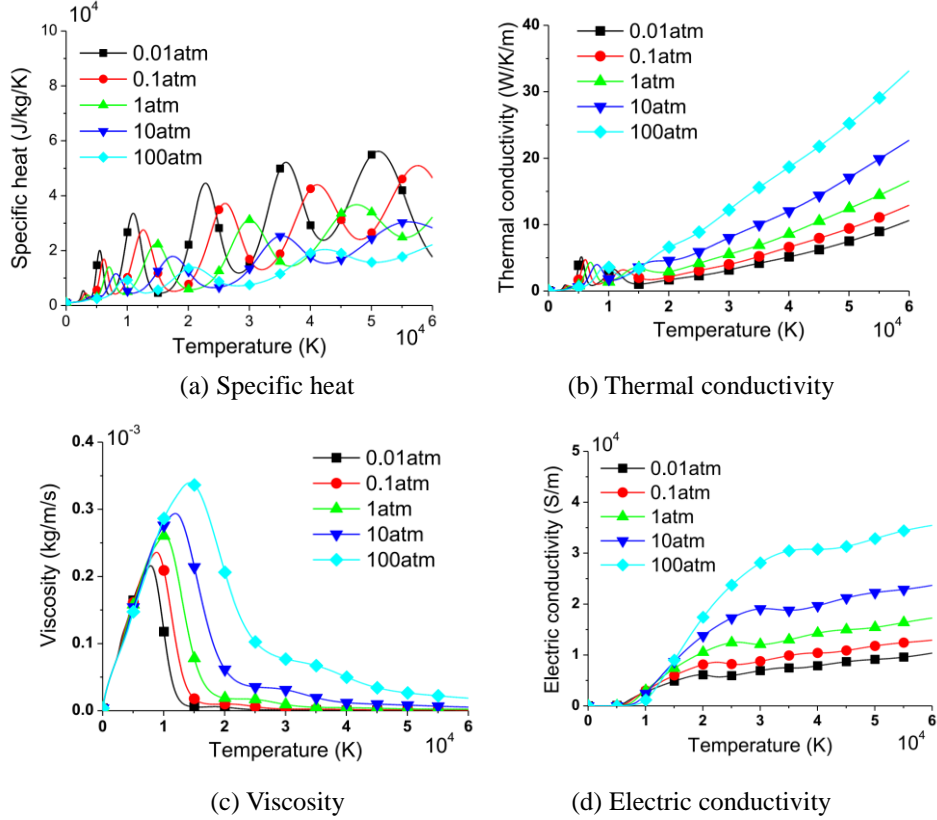


Fig. 5 LTE properties of plasma gas at different pressure and temperature

2.1.3 Resistor-inductor-capacitor (RLC) electrical model

In a very short time step, the voltage across the plasma region can be assumed to be constant. The spark discharge circuit can be regarded as a typical RLC circuit, as shown in Fig. 6. The time dominant model of discharge circuit is established, as shown below.

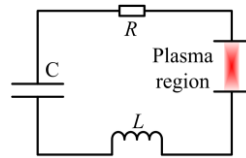


Fig. 6 Simplified discharge circuit

$$\begin{cases} \frac{di(t)}{dt} = \frac{1}{L} [u(t) - Ri(t) - u_s(t)] \\ \frac{du(t)}{dt} = -\frac{1}{C} i(t) \end{cases} \quad (10)$$

In this equation, $u(t)$ is the voltage across the capacitor; R is the total resistance of wire and

equivalent series capacitor resistance; u_s is the voltage across the plasma region, which is calculated by equation (2); C is the capacitance, L is the wire inductance.

2.2 Model solution

2.2.1 Solution method

To solve this model, commercial software FLUENT is adopted. The computation mesh created with ANSYS ICEM is fully structured. The computation domain is shown in Fig. 7. As the electrode radius is larger than the electrodes gap distance, the sphere electrode can be simplified as parallel plate electrode. Considering the high turbulence produced by discharge heating, RSM turbulence model is adopted, which has been validated to produce more accurate results than other models^[42]. The potential conservation equation, axial and radial vector potential conservation equations are solved using user-defined scalar (UDS) approach offered by FLUENT software. User-defined functions are adopted to calculate some necessary parameters appearing in the equations, such as B_0 , j_x , j_r and so on. The gas thermal state model is established using the real gas model offered by FLUENT. Considering the compressibility of plasma flow, the coupled algorithm is adopted and the numerical scheme is implicit in time with the time step size set as 1 ns. To capture the shock wave, the second upwind discretization is used in pressure terms, momentum and energy equations.

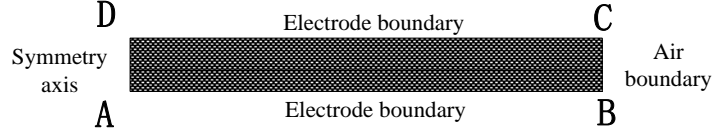


Fig. 7 Computation domain

2.2.2 Boundary conditions

The boundary conditions used in two dimensions are given in table (1), where k is the thermal conductivity of electrode material; T is the temperature at the electrode internal surfaces; T_0 is the temperature of the external surfaces of the sidewalls, which is assumed to be approximately the environmental temperature (300K); d is the thickness of the electrodes.

Table 1 Boundary conditions for the 2D arc model

	P	v_x	v_r	T	V	A_x	A_r
AB	—	0	0	$q = -k(T - T_0)/d$	0 or J_r	$\frac{\partial A_x}{\partial \vec{n}} = 0$	$\frac{\partial A_r}{\partial \vec{n}} = 0$
CD	—	0	0	$q = -k(T - T_0)/d$	J_r or 0	$\frac{\partial A_x}{\partial \vec{n}} = 0$	$\frac{\partial A_r}{\partial \vec{n}} = 0$
AD	$\frac{\partial p}{\partial r} = 0$	$\frac{\partial v_x}{\partial r} = 0$	$\frac{\partial v_r}{\partial r} = 0$	$\frac{\partial T}{\partial r} = 0$	$\frac{\partial V}{\partial r} = 0$	$\frac{\partial A_x}{\partial r} = 0$	$\frac{\partial A_r}{\partial r} = 0$
BC	1 atm	—	—	300 K	$\frac{\partial V}{\partial \vec{n}} = 0$	0	0

The current density is difficult to be calculated accurately. The current density distribution J_i on cathode electrode surface must satisfy the equation (11), where A_i is the area of the boundary elements. For an axial symmetry configuration, this condition can be expressed as equation (12). So the general solution of this condition is given in equation (13). In this paper, the coefficient α_i is given by equation (14), where σ_r is the electrical conductivity of plasma region element near the cathode, r_c is the cathode spot radius, which varies with the charge current. In this paper, the cathode spot radius r_a is calculated by equation (15), which is a fitting function from the research results of Zhou and Heberlein^[37]. The fitted results are plotted in Fig. 8.

$$\sum_{i=1}^n J_i A_i = I \quad (11)$$

$$\int_0^r J_i 2\pi r dr = I \quad (12)$$

$$J_i = \frac{I \alpha_i}{\int_0^{r_a} \alpha_i 2\pi r dr} \quad (13)$$

$$\begin{cases} \alpha_i = \sigma_r \delta(r) \\ \delta(r) = \begin{cases} 1 & r \leq r_a \\ 0 & r > r_a \end{cases} \end{cases} \quad (14)$$

$$r_a = \begin{cases} 3.557 \times 10^{-5} I^{0.628} - 1.237 \times 10^{-6} I + 1.226 \times 10^{-4} & I \geq 5A \\ 2 \times 10^{-4} & I < 5A \end{cases} \quad (15)$$

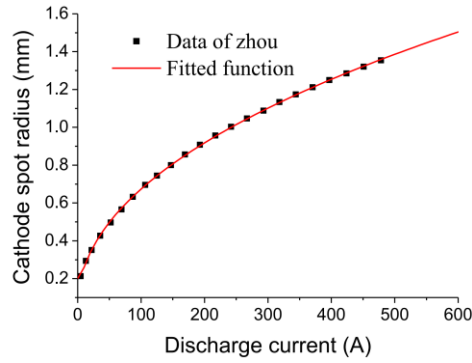


Fig. 8 Cathode spot radius at different discharge currents

2.2.3 The two-equation solving method

Since the physical process of the anode and cathode is different, the boundary type of potential conservation equation for the anode and cathode must be different. In the MHD simulation, potential boundary type of the anode electrode is a zero potential condition, while the cathode electrode is a current density condition. In the traditional arc simulation, the polarity of the electrode is fixed. But for the capacitive discharge simulated in this paper, the polarity of each electrode depends on the current direction. So the potential type at the electrode boundary changes alternately between zero potential condition and current density condition. But the boundary type can't change automatically based on discharge current in the commercial CFD software. When the simulation starts, the boundary type must be chosen between a value condition (a potential value) and a flux condition (a current density). To solve this deficiency, a two-equation method is put forward to solve the potential conservation equation.

At present, the majority of the commercial CFD software offers interface to solve the user-defined conservation equation. In the software, one conservation equation is regarded as an equation to be solved. To solve boundary type alternating process, a two-equation method is put forward. The core of this method is that one conservation equation is divided into two sub-equations to solve. The boundary conditions of the two equations are different. Only one result solved by the two equations is chosen as

the accurate results based on some additional conditions.

In order to solve the anode and cathode alternating process, two user-defined conservation equations about the potential conservation equation is set in the commercial CFD software, and two different potential boundary condition types are set. But only one result is chosen as the ~~true~~ real potential field, which is determined by the discharge current.

2.2.4 Initial condition

Air breakdown is a complex process, which is not considered in this discharge model. This simulation starts just after breakdown of the air between the electrodes, using the conditions at the end of the breakdown as the initial conditions. The initial plasma diameter is taken as 0.5 mm, and the plasma temperature is set to 8000 K. At $t=0$, the velocity and the density of all the grids are taken as 0 m/s and 1.17 kg/m^3 , respectively. Besides, the corresponding pressure is calculated by using the gas thermal state equation.

2.3 Model validation

To validate the simulation model, an experiment system is built, as shown in Fig. 9. A capacitive power supply is connected to electrodes. A DC power supply (0-10kV) is adopted to charge the capacitor. To ensure the discharge energy is only the energy stored in the capacitor. A large current limiting resistor (10 M Ω) is adopted. The capacitance and the breakdown voltage determine the discharge energy. To improve the accuracy of the experimental data, the discharge electrodes are made of two stainless steel spheres. The diameter of the sphere is up to 25mm, larger than the electrode gap distance. The two steel spheres are fixed on two micro positioning systems (sensitivity 1 μm), respectively. The voltage and the current isare measured by a high-voltage probe (Tektronix, P6015) and a current probe (Pearson, 6600), respectively. Measurement points have been illustrated in Fig. 9. An oscilloscope (Tektronix, DPO4014) is used to display and record the data. In this experiment, the capacitor is 2.2 nF, the inductance is 1.01 μH , the total value of wire resistance and equivalent series capacitor resistance is 0.84 Ω . The resistance is obtained by an impedance analyzer (Agilent 4285A).

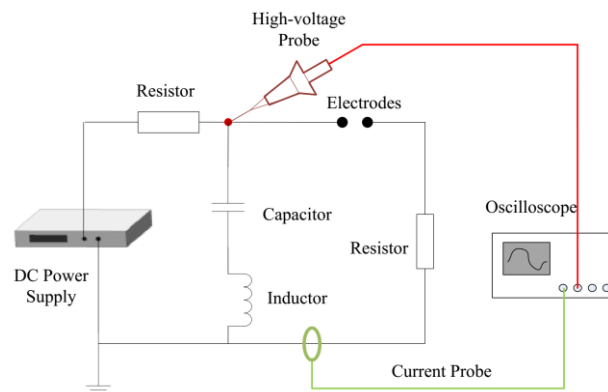


Fig. 9 Experiment system

~~Supposed~~ Assuming that the arc resistance kept unchanged in one oscillation period, the time-independent arc resistance can be calculated based on discharge current, as equation (16). The $I_m(n)$ presents the maximum /minimum current in the n th oscillation period. Based on calculated time-independent arc resistance using the simulation model, the average resistance in an oscillation period is calculated based on equation (17). As shown in Fig. 10, the calculated results show a good agreement with the experiment results.

$$R_{arc}(n) = -\ln\left(\frac{I_m(n)}{I_m(n-1)}\right) \cdot \frac{T}{L_t} - R_{wire} \quad (16)$$

$$R_i = \frac{\int_0^T i^2 R(t) dt}{\int_0^T i^2 dt} \quad (17)$$

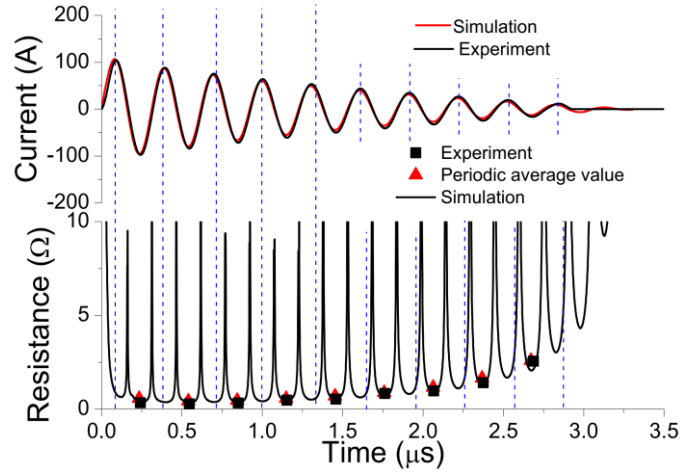


Fig. 10 Model validation

In the entire discharge process, the plasma resistance changes dramatically. In the initial discharge stage, a sharp drop is shown. During the zero-crossing of the AC current, the resistance increases quickly. What's more, as the resistance increases in the later discharge stage, the decay factor increases. As a result, the oscillation vanishes quickly. This typical phenomenon in the discharge process is well caught by the simulation model.

3 Simulation results and analysis

As a critical process during the working cycle of the PSJA, the discharge process plays a key role on the efficiency of the PSJA. Based simulation results, the influence of sheath energy loss, radiation loss, and thermodynamic energy loss is studied below. Based on these results, some design advices on PSJA are given.

3.1 Sheath energy loss

In the previous discharge simulation, it has been confirmed that the sheath dissipates the majority of the energy^{[27][28]}. To strengthen understanding, the quantitative analysis of sheath energy loss and the relationship with the discharge time are made.

In this MHD-RLC discharge model, the voltage fall of sheath region and the arc column is shown in Fig. 11 with a 2.2 nF capacitor. Before 500 ns, the voltage fall of arc column is larger than that of sheath region. But soon after, the voltage fall of the arc column decreases. Meanwhile, the voltage fall of sheath region changes a little. The current density for these two regions is equal. So the energy consumed in these two regions is proportional to the voltage fall of these two regions. The energy-loss coefficient of the sheath region is 41%, which is calculated by equation (18).

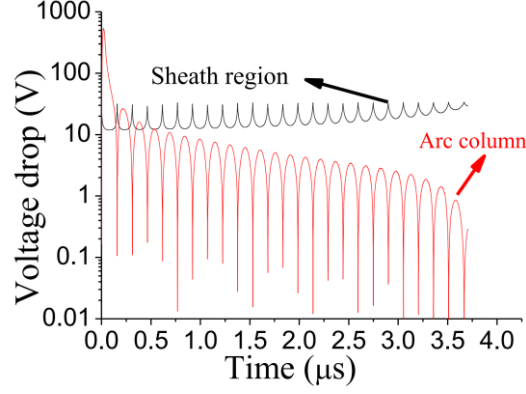


Fig. 11 Voltage history of sheath region and arc column

$$\zeta = \frac{\int u_{sheath} idt}{\int (u_{arc} + u_{sheath}) idt} \quad (18)$$

As shown from Fig. 11, the sheath energy loss increases with the discharge time. Calculated by equation (17), the sheath energy loss coefficient versus discharge time is obtained, which is shown in Fig. 12. By the least squares fit, this relationship can be expressed as equation (19). Therefore, if the discharge time can be reduced by a quick switch, the sheath energy loss decreases by exponential law. For example, along with the discharge time reduced to 100 ns, the sheath energy loss decreases to only 7%. This result is similar with that of Zhu Y.^[43], which has shown that the deposited energy decreases with increase of the voltage rise time. The increase of voltage rise time leads to the increase of discharge time.

$$\zeta = -0.3778 \exp(-9.291E5 \times t) + 0.4182 \quad (19)$$

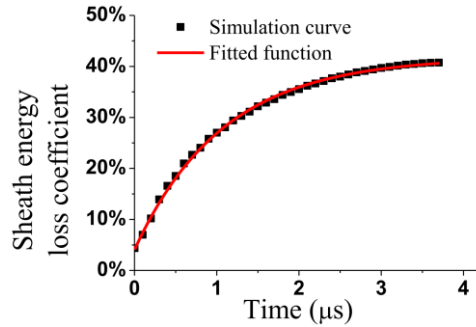


Fig. 12 The time-dependent sheath energy loss coefficient

With different capacitance and inductance, the sheath energy loss is different, which is shown in Fig. 13. With the increase of the inductance and the capacitance, the energy loss coefficient increases. The inductance determines the energy deposition speed. With the increase of inductance, the energy deposition speed decreases, prolonging the discharge time. As a result, the sheath energy loss coefficient increases. With the increase of capacitance, the energy stored in the capacitor increases. When the energy deposition speed keeps unchanged, longer discharge time is necessary. Naturally, the sheath energy loss coefficient increases as well.

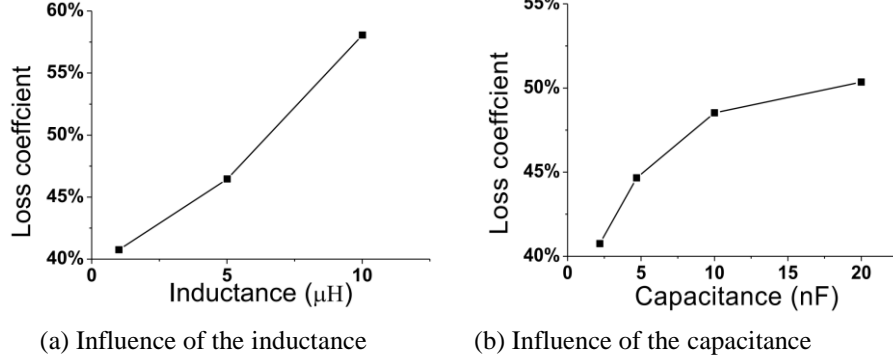


Fig. 13 The sheath energy loss coefficient with different capacitance and inductance

3.2 Radiation loss

Based on the Plank radiation law, the thermal radiation power is proportional to 4th power of the temperature. The temperature in the plasma would increase up to 10000K. Thus, the thermal radiation can't be ignored. The radiative loss with different capacitance and inductance is shown in Fig. 14. The radiation loss power increases when the capacitance increases and the inductance decreases. The radiation loss energy can be calculated by computing the integral of the radiation loss power. The radiation loss coefficient is defined as equation (20). The calculated results are plotted in Fig. 15. The difference of the radiation loss coefficient for different capacitances is not significant. Only when the inductance increases, the radiation loss coefficient decreases. However, comparing with the sheath energy loss coefficient, the radiation loss coefficient is small, which agrees with the simulation results of Dufour^[18].

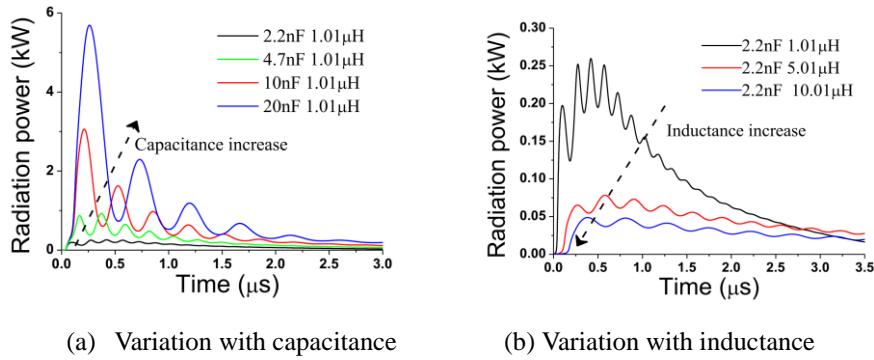


Fig. 14 The variation of radiative loss with different capacitance and inductance

$$\eta_{\text{radiation}} = \frac{Q_{\text{radiation}}}{\int (u_{\text{arc}} + u_{\text{sheath}}) idt} = \frac{\int P_{\text{radiation}} dt}{\int (u_{\text{arc}} + u_{\text{sheath}}) idt} \quad (20)$$

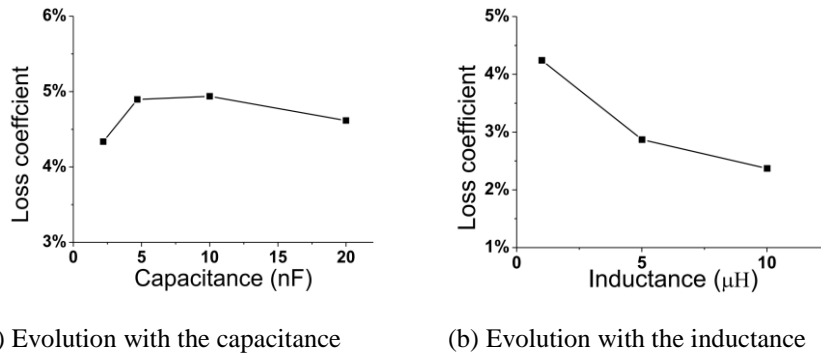


Fig. 15 Evolution of radiation loss coefficient for different capacitance and inductance

3.3 Thermodynamic loss

It is known that the discharge process is the source of heating. Based on the thermodynamic theory, compared with the constant pressure heating process, the constant volume heating process is more efficiency to increase the mechanical energy of the gas.

The polytropic index is used to identify the heating process, which is calculated by equation (21), where the subscript 1 stands for the initial state. The initial pressure and density are 1 atm and 1.17 kg/m³ in this paper. As plasma ohm heating is determined by gas electric characteristics, the plasma ohm heating region is defined as the region where the gas electric conductivity is larger than 10 S/m. Then, the average density and pressure in the heating region can be calculated by equation (22), where A is the fluid field region. The polytropic index history is presented in Fig. 16. In the entire energy deposition process, the polytropic index increases quickly and stays to 0 at about 100 ns. That is to say, the energy deposition process transfers from a constant volume heating process to a constant pressure heating process quickly.

$$n = \frac{\log(P_2 / P_1)}{\log(\rho_2 / \rho_1)} \quad (21)$$

$$\left\{ \begin{array}{l} P = \frac{\iint_A \delta(\sigma) P dA}{\iint_A \delta(\sigma) dA} \\ \rho = \frac{\iint_A \delta(\sigma) \rho dA}{\iint_A \delta(\sigma) dA} \\ \delta(\sigma) = \begin{cases} 1 & \sigma \geq 10 \\ 0 & \sigma < 10 \end{cases} \end{array} \right. \quad (22)$$

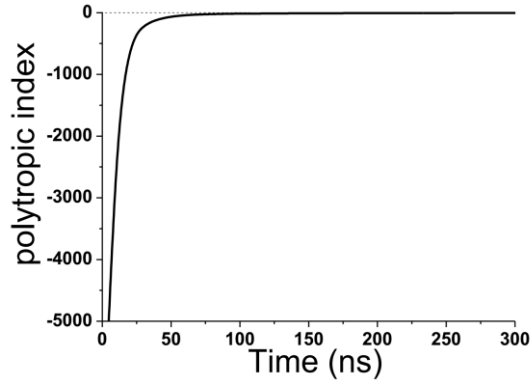


Fig. 16 Polytropic index history

Actually, the ~~true~~ heating region is just a small region between the electrodes, which only occupies a small part of the PSJA chamber volume. Therefore, the heating process is in an open environment. Nevertheless, owing to the air inertia, if the energy deposition process is quick enough, the air will not have enough time to expand. In Fig. 17, the pressure contour, density contour and heating region at different time step are presented in order, from the left to the right. As the gas breakdown occurs, the arc center presents a high pressure state. Then a strong shock wave forms. The shock wave is a strong compression wave, where the density is larger than that of the ambient gas. As

the shock wave moves, the density of the plasma region decreases. That is to say, since then the heating process can't be seen as a constant volume heating process. The heating process has transferred from constant volume heating process to constant pressure heating process. Since then, the majority of the deposited energy is transferred to gas thermal energy instead of mechanical energy.

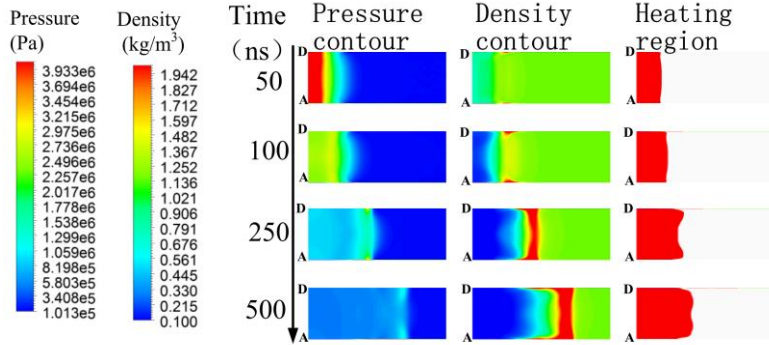


Fig. 17 Pressure density contours and heating region at different time step

3.4 Influence of the energy deposition speed

As discussed above, the thermodynamic cycle efficiency is not a constant, but will decrease with the heating time. If the influence of the energy deposition speed on the efficiency is analyzed coupled with the thermodynamic cycle efficiency, more information about the low efficiency of PSJA is obtained.

Actually, the energy deposition speed is not constant as well. The energy deposition power history versus different groups of capacitance and inductance is shown in Fig. 18, which is calculated by equation (23). When the inductance keeps constant, the energy deposition power history at the initial time is almost the same. As the capacitor increases, the maximum power increases only a little. The main difference induced by large capacitor is the energy deposition speed at the later stage. In detail, when the capacity increases, the deposited energy at the initial stage doesn't increase significantly. But the deposited energy at the later stage increases significantly. That is to say, the majority of the increased energy deposited in a constant pressure heating process. Naturally, the efficiency decreases. When the capacitance keeps unchanged, with the increase of inductance the energy deposition power decreases quickly, which is harmful to the efficiency.

This phenomenon agrees well with the research results of A. Belinger's group^[44]. The inductive power discharge has higher discharge efficiency, can deposit more energy into the air, but produces weaker synthetic jet, comparing with the capacitive discharge. To the capacitive discharge, the inductance of the circuit has similar effect on the performance of PSJA. The lower the inductance is, the higher efficiency is.

$$Q = \iint_A \frac{j_x^2 + j_r^2}{\sigma} 2\pi r dA \quad (23)$$

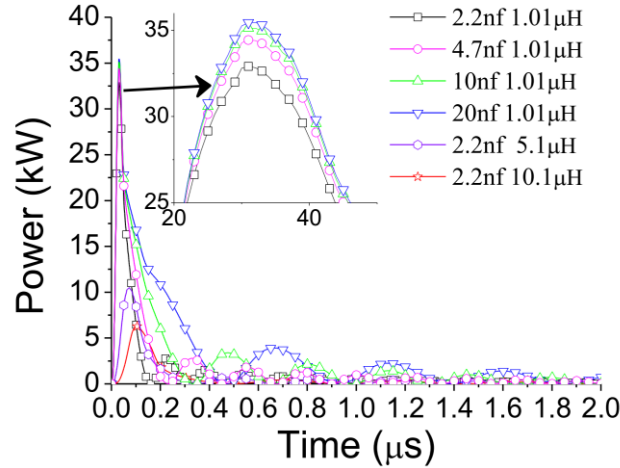


Fig. 18 Time-dependent heating power for different capacitance and inductance

In summary, similar as the previous research, the efficiency would decrease with the increase of the capacitance. The reason is not just the arc column resistance decreases with the increase of capacitance. The low thermodynamic efficiency is another important reason. When the capacitance increases, more energy releases in the later stage of the discharge process. At this time, the heating process has nearly transferred to a constant pressure heating process, which has low thermodynamic cycle efficiency. These factors aggravate the decrease of efficiency. So the capacitance should choose a low value. When the capacitance is fixed, the value of the inductance should be as low as possible. What's more, if the discharge time can be controlled by a quick solid-state switch, the energy efficiency can be improved greatly.

4 Conclusions

In this paper, an arc discharge model is established, which couples MHD equations with the RLC circuit equations. To improve the model accuracy, the magnetic force induced by discharge current, the real gas effect, the sheath voltage fall, the radiation loss etc. are taken into consideration. Based on the simulation results, the characteristics of transforming electrical energy to mechanical energy are studied. The main conclusions are as follows.

During the process of discharge energy transforming to the gas thermal energy, the sheath energy loss coefficient ranges from 40% to 60%, while the radiation loss coefficient is less than 5%. The sheath energy loss coefficient is not constant. With the decrease of the discharge time, the sheath energy loss decreases by exponential law. When the discharge time reduced to 100 ns, the sheath energy loss coefficient reduces to less than 10%.

The thermodynamic efficiency is not constant as well. With the increase of discharge time, the heating process changes from a constant volume heating process to a constant pressure heating process, causing the thermal efficiency decreases.

In the capacitive discharge process, the inductance plays a determinant role on the energy deposition speed, and the capacitor coupled with the voltage determines the energy stored in the capacitor. With the increase of capacitance, the energy increases. However, the majority of the increased energy deposits in a constant pressure heating stage, which is characterized by low thermodynamic cycle efficiency. The energy deposited in the constant volume heating stage doesn't increase linearly. The characteristic aggravates the low efficiency of the discharge with large capacitive.

In this paper, only the discharge process of the PSJA is studied. In the future, the entire working

process of the PSJA will be studied and more characteristics about the energy efficiency would be researched.

ACKNOWLEDGMENTS

This work was sponsored by the National Natural Science Foundation of China (91541120,51522606, 51336011, 51611130198, 51407197 and 11472306).

REFERENCES

- [1] Saha Ashish S. Sharma Vikram. Numerical Investigations on Flow Control over Blended-Wing-Body Transonic Aircraft Using Synthetic-Jet Actuators[J]. *Journal of Aircraft*, 2012,49(2):532-545
- [2] Tesař V., Trávníček Z., Kordík J., et al. Experimental investigation of a fluidic actuator generating hybrid-synthetic jets[J]. *Sensors and Actuators a: Physical*, 2007,138(1):213-220.
- [3] Tesař V. Configurations of fluidic actuators for generating hybrid-synthetic jets[J]. *Sensors and Actuators a: Physical*, 2007,138(2):394-403
- [4] Tesař V., Zhong S., Rasheed F. New Fluidic-Oscillator concept for Flow-Separation control[J]. *AIAA Journal*,51(2):397.
- [5] Tesař V. Measuring unsteady axial velocity of fibres and threads[J]. *Sensors and Actuators a: Physical*, 2009,155(1):89-97
- [6] Zhang C, Wang Y, et al. Electrical Characteristics in Surface Dielectric Barrier Discharge Driven by Microsecond Pulses. *IEEE TRANSACTIONS ON PLASMA SCIENCE*,2016,44,2772-2778
- [7] Jiang Hui, Shao Tao, Zhang Cheng, et al. Experimental study of Q-V Lissajous figures in nanosecond-pulse surface discharges[J]. *IEEE Transactions On Dielectrics and Electrical Insulation*, 2013,20(4):1101-1111
- [8] Shao Tao, Jiang Hui, Zhang Cheng, et al. Time behaviour of discharge current in case of nanosecond-pulse surface dielectric barrier discharge[J]. *Europhysics Letters (EPL)*, 2013,101(4):45002.
- [9] Zhang Z, Wu Y, Jia M, et al. Influence of the discharge location on the performance of a three-electrode plasma synthetic jet actuator. *Sensors and Actuators A: Physical*, 2015, 235: 71-79.
- [10] Zong H, Wu Y, Jia M, et al. Influence of geometrical parameters on performance of plasma synthetic jet actuator, *J. Phys. D: Appl. Phys.* 49 (2016) Zong H, Wu Y, Jia M, et al. Influence of geometrical parameters on performance of plasma synthetic jet actuator. *Journal of Physics D: Applied Physics*, 2015, 49(2): 025504
- [11] Narayanaswamy V, Raja L L, Clemens N T. Control of unsteadiness of a shock wave/turbulent boundary layer interaction by using a pulsed-plasma-jet actuator. *Physics of Fluids* , 2012, 24(7): 076101.
- [12] Narayanaswamy V, Raja L L, Clemens N T. Control of a shock/boundary-layer interaction by using a pulsed-plasma jet actuator, *AIAA journal*, 2012, 50(1): 246-249.
- [13] II T M E, Ali M Y, Foster C H, et al., SparkJet Actuator Characterization in Supersonic Crossflow, 6th AIAA Flow Control Conference, AIAA 2012-2814
- [14] Emerick T, Ali M Y, Foster C, et al. SparkJet characterizations in quiescent and supersonic flowfields. *Experiments in Fluids*, 2014, 55(12): 1-21
- [15] Anderson K V, Knight D D. Plasma jet for flight control. *AIAA journal*, 2012, 50(9): 1855-1872.
- [16] Haack S J, Taylor T M, Cybyk B Z, et al. Experimental estimation of sparkjet efficiency, 42nd AIAA Plasmadynamics and Lasers Conference. 2011, 3.

- [17] Golbabaei-Asl M, Knight D, Wilkinson S. Novel technique to determine sparkjet efficiency. *AIAA Journal*, 2014, 53(2): 501-504.
- [18] Dufour G, Hardy P, Quint G, et al. Physics and models for plasma synthetic jets. *International Journal of Aerodynamics*, 2013, 3(1-2-3): 47-70.
- [19] Lin W, Zhen-Bing L, Zhi-Xun X, et al., Energy efficiency and performance characteristics of plasma synthetic jet, *Acta Phys. Sin.* 62(12) (2013),125207
- [20] Cybyk B Z, Wilkerson J T, Grossman K R, et al., Computational assessment of the sparkjet flow control actuator, Orlando, Florida,AIAA 2003-3711,2003
- [21] K. R. Grossman, B. Z. Cybyk and M. C. Rigling, et al, Characterization of sparkjet actuators for flow control,AIAA 2004-89,2004
- [22] B. Z. Cybyk, J. T. Wilkerson and K. R. Grossman, Performance Characteristics Of The Sparkjet Flow Control Actuator,AIAA 2004-2131,2004
- [23] B. Z. Cybyk, K. R. Grossman and J. T. Wilkerson, et al, Single-pulse performance of the sparkjet flow control actuator,AIAA 2005-401,2005
- [24] B. Z. Cybyk, J. T. Wilkerson and D. H. Simon, Enabling high-fidelity modeling of a high-speed flow control actuator array,AIAA 2006-8034,2006
- [25] T. M. Taylor and B. Z. Cybyk, High-fidelity modeling of micro-scale flow-control devices with applications to the macro-scale environment,AIAA 2008-2608,2008
- [26] P. Hardy, P. Barricau and A. Belinger, et al, Plasma synthetic jet for flow control,AIAA 2010-5103,2010
- [27] G. Sary, G. Dufour and F. Rogier, et al,Modeling and Parametric Study of a Plasma Synthetic Jet for Flow Control,AIAA J. 52(8)(2014),1591-1603
- [28] F. Laurendeau, F. Chedevigne and G. Casalis,Transient ejection phase modeling of a Plasma Synthetic Jet actuator,PHYS FLUIDS 26(2014), 125101
- [29] Xu G, Hu J, Tsai H L. Three-dimensional modeling of the plasma arc in arc welding. *Journal of Applied Physics*, 2008, 104(10): 103301.
- [30] Menart J, Lin L. Numerical study of high-intensity free-burning arc. *Journal of thermophysics and heat transfer*, 1998, 12(4): 500-506
- [31] O. Ekici, R. Matthews and O. Ezekoye,Geometrical and electromagnetic effects on arc propagation in a railplug ignitor,*Journal of Physics. D, Applied Physics* 40(24)(2007),7707-7715
- [32] M. Schnick, U. Fuessel and M. Hertel, et al,Numerical investigations of arc behaviour in gas metal arc welding using ANSYS CFX,*Frontiers of Materials Science* 5(2)(2011),98-108
- [33] P. Freton, J. J. Gonzalez and A. Gleizes,Comparison between a two- and a three-dimensional arc plasma configuration,*Journal of Physics D: Applied Physics* 33(19)(2000),2442-2452
- [34] H. L. F. L. Qianhong Zhou,Effects of Nozzle Length and Process Parameters on Highly Constricted Oxygen Plasma Cutting Arc,PLASMA CHEM PLASMA P. 28(6)(2008),729-747
- [35] Y. Wu, M. Rong and Z. Sun, et al,Numerical analysis of arc plasma behaviour during contact opening process in low-voltage switching device,*Journal of Physics D, Applied Physics* 40(3)(2007)
- [36] O. Ekici, R. Matthews and O. Ezekoye,Geometrical and electromagnetic effects on arc propagation in a railplug ignitor,*Journal of Physics. D, Applied Physics* 40(24)(2007),7707-7715
- [37] Zhou X, Heberlein J. Analysis of the arc-cathode interaction of free-burning arcs. *Plasma Sources Science and Technology*, 1994, 3(4): 564.
- [38] R. Hemmi, Y. Yokomizu and T. Matsumura,Anode-fall and cathode-fall voltages of air arc in

- atmosphere between silver electrodes.,*Journal of Physics D, Applied Physics* 36(9)(2003),1097-1106
- [39] Y. Naghizadeh-Kashani, Y. Cressault and A. Gleizes, Net emission coefficient of air thermal plasmas, *Journal of Physics D: Applied Physics* 35(22)(2002),2925–2934
- [40] H. L. F. L. Qianhong Zhou, Effects of Nozzle Length and Process Parameters on Highly Constricted Oxygen Plasma Cutting Arc, *PLASMA CHEM PLASMA P.* 28(6)(2008),729-747
- [41] A. D'Angola, G. Colonna, C. Gorse and M. Capitelli, Thermodynamic and transport properties in equilibrium air plasmas in a wide pressure and temperature range, *The European Physical Journal D - Atomic, Molecular and Optical Physics* 46(1)(2008),129–150
- [42] Q. Zhou, H. Li and X. Xu, et al, Comparative study of turbulence models on highly constricted plasma cutting arc, *Journal of Physics D: Applied Physics* 42(1)(2009)
- [43] Zhu Y, Wu Y, Jia M, et al. Influence of positive slopes on ultrafast heating in an atmospheric nanosecond-pulsed plasma synthetic jet. *Plasma Sources Science and Technology*, 2014, 24(1):015007
- [44] A. Belinger, P. Hardy and P. Barricau, et al, Influence of the energy dissipation rate in the discharge of a plasma synthetic jet actuator, *JOURNAL OF PHYSICS D: APPLIED PHYSICS*(2011)